Journal of Molecular Structure 1334 (2025) 141764

Contents lists available at ScienceDirect

Journal of Molecular Structure

journal homepage: www.elsevier.com/locate/molstr

From cigarette filters to photocatalysts: Self-carbon-doped ZnO for effective water remediation

Yasemin Aytac [a], Nazli Turkten [b], Dila Kaya [a,*]

[a] Department of Chemistry, Faculty of Engineering and Natural Sciences, Istanbul Medeniyet University, Istanbul, 34700, Turkiye
[b] Department of Chemistry, Faculty of Arts and Sciences, Kirsehir Ahi Evran University, Kirsehir, 40100, Turkiye

ARTICLE INFO

Keywords:
Carbon-doped ZnO
Cigarette filter
Methylene blue
Photocatalysis
Self-doping

ABSTRACT

A simple strategy was presented to convert a possibly problematic and harmful solid waste into a sustainable and feasible value-added product. In this regard, novel self-carbon-doped ZnO (C-ZnO) photocatalysts containing both unground cigarette filters (CF) and ground cigarette filters (CFG) as carbon sources and templates were successfully synthesized for the first time. A series of C-ZnO photocatalysts containing three different amounts of CF and CFG were obtained by a facile one-step precipitation method. Comprehensive characterization of C-ZnO photocatalysts was realized via FTIR, Raman, XRD, SEM-EDAX, TGA, BET, and PL analysis techniques. While the grinding process did not affect the structural and crystallite properties of the templates, differences were observed in CF and CFG morphology. The crystallite sizes of C-ZnO photocatalysts differed depending on the CF and CFG amounts used as templates. The as-prepared specimens were used as promising photocatalysts for the remediation of methylene blue (MB) contaminated water. C-ZnO photocatalyst with the lowest CFG amount, denoted as 0.06-CFGZ exhibited high MB degradation (98 %) under 270 min irradiation. Amounts of CF and CFG in C-ZnO photocatalysts influenced their morphology, playing an important role in their photocatalytic activities. The design of C-ZnO using CF and CFG templates not only facilitated the valorization of environmental waste but also offered a novel strategy for the preparation of efficient carbon-doped photocatalysts.

1. Introduction

Due to rapid population growth and increasing industrial processes, the demand for drinking water and effective wastewater treatment methods is increasing. The effluents of some industries and their products pollute water resources to such an extent that they affect human life. Wastewater from textile, leather, cosmetics, and paper industries contains significant amounts of dye effluents. Among cationic textile dyes, methylene blue (MB) is a relatively low toxic thiazine dye that can cause adverse effects on human health. Additionally, the presence of this non-biodegradable compound in aquatic systems can block sunlight and reduce the availability of dissolved oxygen. Therefore, wastewater treatment containing this dye is crucial before discharging into water bodies and the environment [1–3].

Recently, wastewater treatment technologies including adsorption [4,5], ionic flocculation [6], membrane filtration [7] and bioaccumulation [8] have been applied to eliminate this aromatic heterocyclic dye. Most conventional approaches have drawbacks, including the disposal of exhausted adsorbent causing secondary pollution and an extended retention time required for biodegradation of complex and recalcitrant dye. Alternatively, advanced oxidation processes (AOPs) can be performed as notable methods to degrade MB to harmless substances such as CO_2 and H_2O. There are different ways of incorporating AOPs into water treatment but they work on the same principle: reactive oxygen species are generated in an aqueous environment and take part in oxidative processes. AOPs can be implemented for oxidative degradation of organic and inorganic pollutants as well as inactivation of pathogens. Among AOPs, photocatalysis is a cost-effective, energy-saving, and environmentally friendly water treatment method that generates various reactive species, including but not limited to hydroxyl radicals, to eliminate organic pollutants through a non-selective oxidation mechanism [9–11].

ZnO has drawn attention as a promising photocatalyst in recent decades due to its properties such as being low-cost, non-toxic, and biocompatible. However, the wide band gap energy and rapid electron-hole pair recombination limit the actual photocatalytic application of this semiconductor [12–14]. To overcome this challenge and improve the photocatalytic efficiency of ZnO, researchers have focused on the use

* Corresponding author.
E-mail address: dila.kaya@medeniyet.edu.tr (D. Kaya).

https://doi.org/10.1016/j.molstruc.2025.141764
Received 17 December 2024; Received in revised form 28 January 2025; Accepted 14 February 2025
Available online 15 February 2025

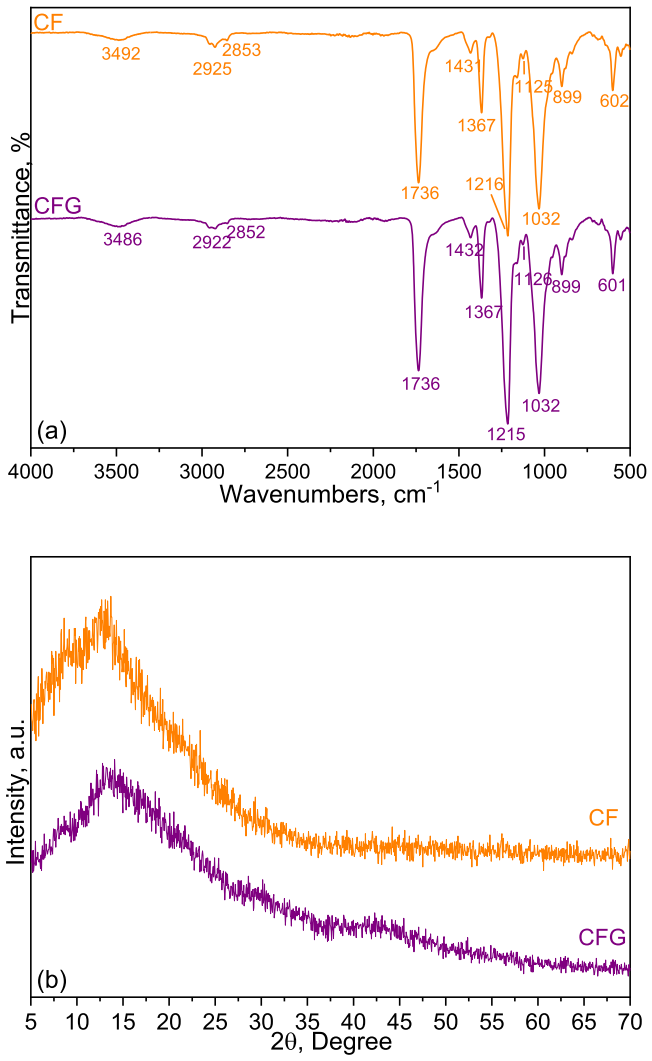

Fig. 1. (a) FTIR spectra (b) XRD diffractograms of CF and CFG specimens.

of combination with other semiconductors [15], preparation of polymeric composites [16,17], and doping with metals and non-metals [18]. Among these strategies, designing new carbon-based ZnO photocatalysts (C-ZnO) has gained importance in utilizing agricultural wastes (psyllium husk), bio-waste (wood wastes, brewed coffee), and plant extract-based natural resources (agro-waste extract) as carbon sources [19–23]. In addition, current studies are carried out on cigarette butts, one of the most commonly available abundant personal waste to that can be converted into a useful product for water treatment [24]. Considering the concept of AOPs in water treatment, this non-biodegradable, toxic waste has been mainly used as a carbon-based solid source to prepare a potential catalyst [25,26].

Gupta and Pandey [26] reported the photocatalytic degradation of MB with carbon containing niobium carbide catalysts synthesized by using filters of smoked cigarettes. As an alternative catalyst, Co and Fe co-doped carbon material was prepared from waste cigarette filters for persulfate oxidation with high COD removal from biological textile wastewater [25]. Glugoski et al. [27] published studies on the utilization of the filters from smuggled cigarettes with immobilized Fe^{3+} for the degradation of Reactive Black 5 dye by the photo-Fenton process. Ultimately, the authors reported that they preferred to use smuggled CFs instead of used filters due to the absence of toxic substances from the combustion of tar and nicotine.

There is a limited number of studies in the literature on using either smoked or pristine cigarette filters as carbon sources in photocatalyst systems. The main novelty of this study is the first-ever presentation of a unique combination of cigarette filters and ZnO systems with two different strategies based on unground and ground filters. Here, the comparison between ground and regular cigarette filters as carbon sources was hypothesized to reveal differences in doping efficiency and the resulting C-ZnO photocatalyst properties through variations in surface area and carbon incorporation mechanisms. These variations could potentially influence the photocatalytic performance of the resulting

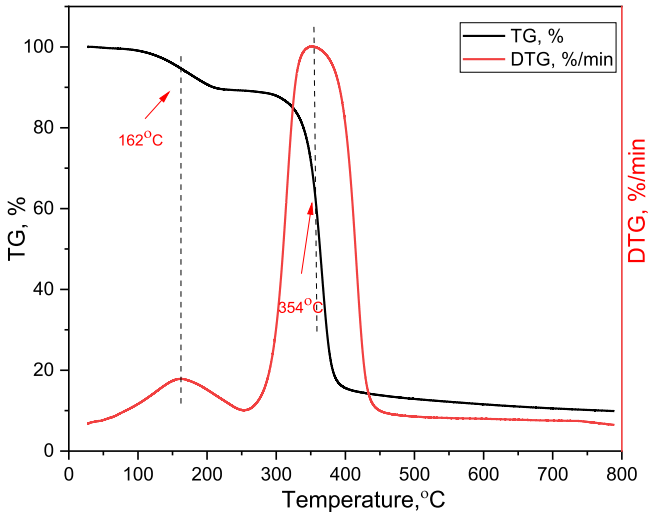

Fig. 3. TG and DTG curves of CFG.

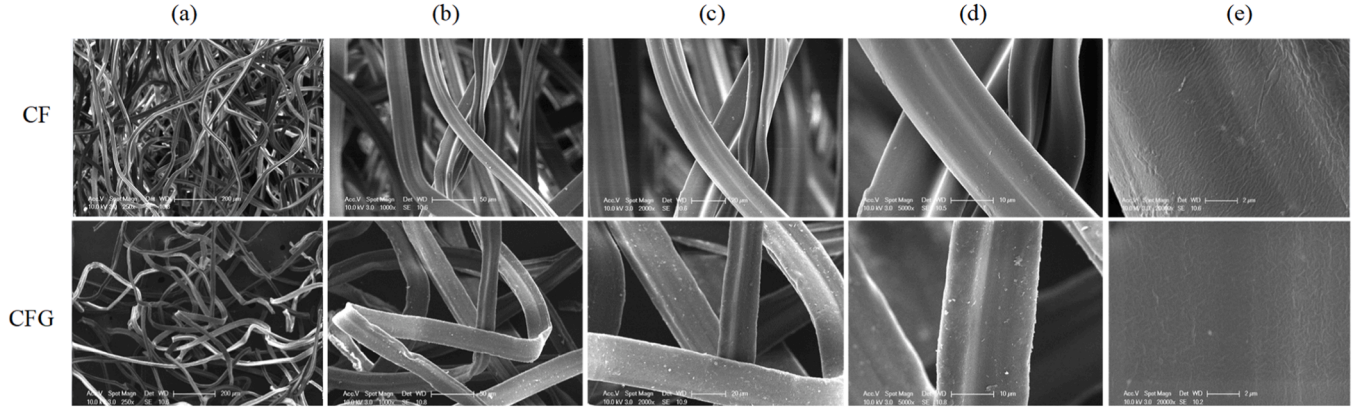

Fig. 2. SEM images of CF and CFG specimens at different magnifications (a) 250x, (b) 1000x, (c) 2000x, (d) 5000x, (e) 20000x.

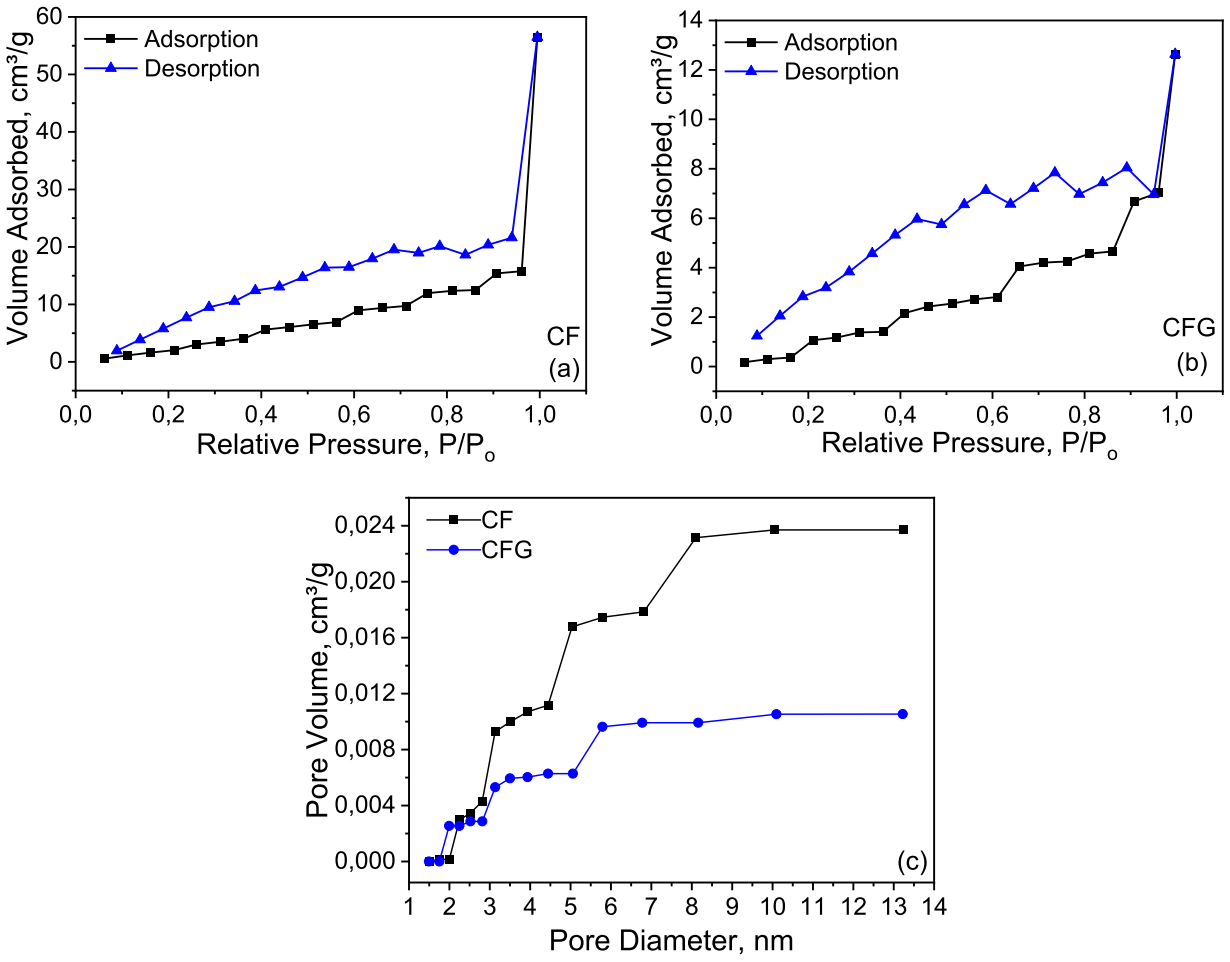

Fig. 4. Nitrogen adsorption-desorption isotherms of (a) CF, (b) CFG, and (c) pore size distribution plots of CF and CFG.

materials. A systematic characterization of photocatalysts was carried out to identify the possible differences in structural, morphological, optical, and surface properties. The photocatalytic activity of the carbon self-doping photocatalysts that enabled dual environmental benefits was investigated using MB as a cationic model dye pollutant.

2. Methodology

2.1. Materials

Cigarettes used in this work had long slim filters (6 mm x 22 mm) that consisted of only cellulose acetate (without any additives). They were obtained in the Turkish market and the filter parts were separated. The reason for using unsmoked cigarette filters was the absence of toxic substances associated with the combustion products. The unground and ground filters were used in two different forms named CF and CFG, respectively. Foss Cyclotec ™ (CT293) device was used with a 1 mm sieve apparatus for the grinding process of the filters. CFG was weighed and used directly for the photocatalyst synthesis while CF was cut into approximately 1 cm pieces.

MB ($C_{16}H_{18}ClN_3S.xH_2O$ (x = 2–3), Merck), zinc nitrate hexahydrate ($Zn(NO_3)_2{\cdot}6H_2O$, reagent grade, 98 %, Merck), and sodium hydroxide (NaOH, ACS reagent, ≥97.0 %, pellets, Sigma-Aldrich) were used without further purification. All solutions were prepared with ultrapure water from the Elga Purelab QUEST UV pure water device.

2.2. Synthesis of photocatalysts

The synthesis of the photocatalysts was carried out using the precipitation method with a minor modification [28]. A series of CF-ZnO and CFG-ZnO photocatalysts were prepared using three different loading amounts of CF and CFG, respectively. The quantities of CF added were 0.06 g, 0.3 g, and 0.6 g, and the resulting photocatalysts were designated as 0.06-CFZ, 0.3-CFZ, and 0.6-CFZ, respectively.

In a typical synthesis of the 0.06-CFZ specimen, 0.1 M Zn $(NO_3)_2{\cdot}6H_2O$ solution (200 mL) was prepared and placed in a flat-bottomed flask. Subsequently, 0.06 g CF was added to this solution with vigorous stirring by a magnetic stirrer for five minutes to obtain a uniform and stable solution (solution A). A solution of 0.1 M NaOH (400 mL) was prepared (solution B) and placed in a dropping funnel. Solution B was added slowly (1 drop/second) to solution A under vigorous stirring. The mixture was stirred for a further 2 h and kept for 24 h at room temperature to obtain precipitates. Then, the white precipitates were filtered and extensively washed with distilled water and ethanol. Subsequently, the rinsed precipitates were dried in an air oven at 80 °C for 24 h, calcined in a 500 °C muffle furnace for 5 h, and ground in an agate mortar. The same procedure was followed for the synthesis of CFGZ specimens, 0.06-CFGZ, 0.3-CFGZ, and 0.6-CFGZ. ZnO nanoparticles were also synthesized for comparison purposes without the addition of CF or CFG.

2.3. Characterization

The structural, morphological, and optical differences between ZnO particles and CFZ and CFGZ specimens were investigated by a range of techniques. Fourier Transform Infrared attenuated total reflectance (FTIR-ATR) analysis was conducted using a Perkin Elmer FTIR Spectrometer Spectrum Two device (diamond/ZnSe crystal Universal ATR

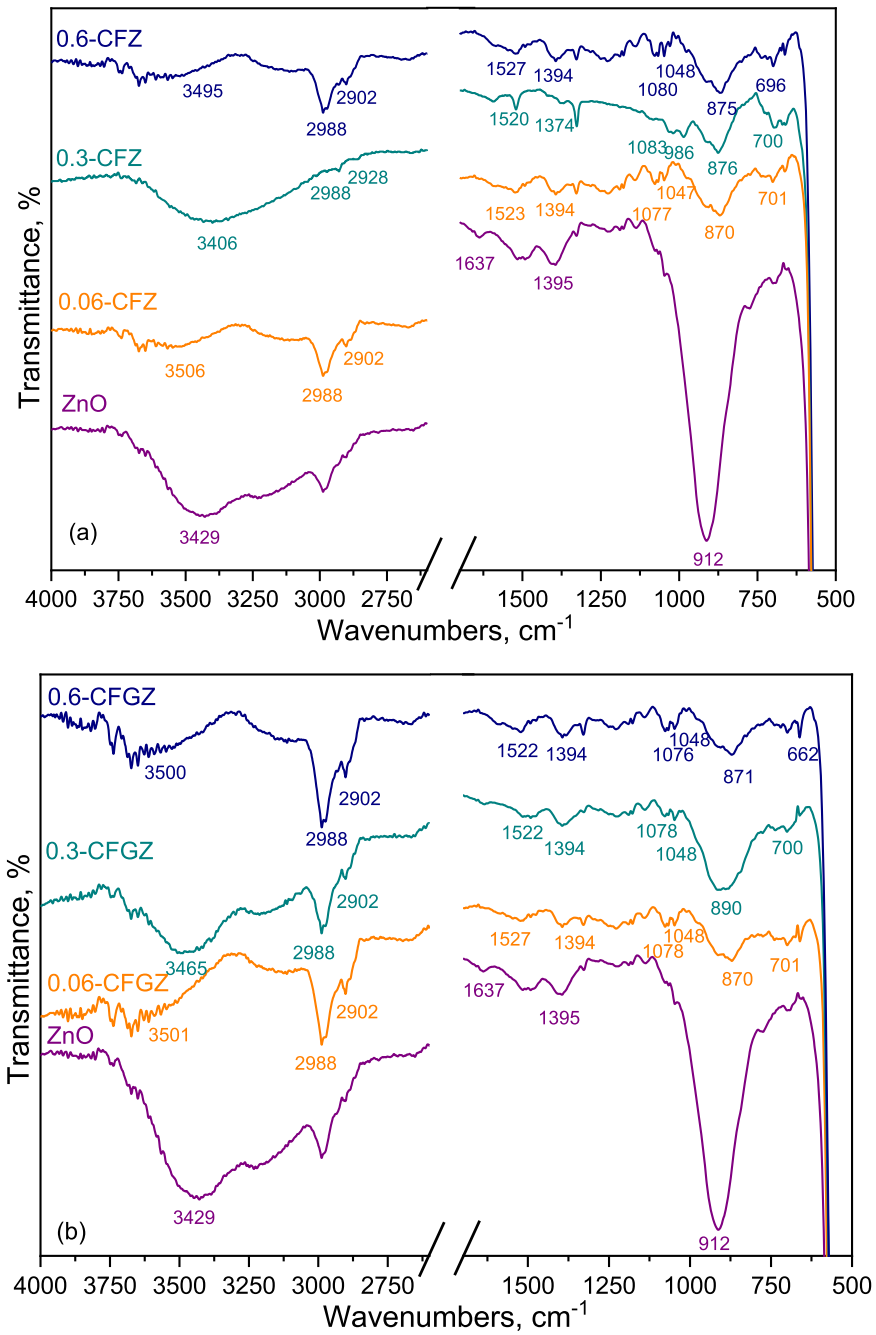

Fig. 5. FTIR spectra of (a) ZnO particles and CFZ photocatalysts, (b) ZnO particles and CFGZ photocatalysts.

accessory) operating in the 4000–400 cm^{-1} region with a resolution of 2 cm^{-1}. Dispersive Raman spectroscopy measurements were carried out using a Thermo Scientific DXR Raman Microscope using laser excitation at λ=532 nm. The spectra were recorded with 2 cm^{-1} spectral resolution and 10 mW Ar^{+} laser power. X-ray diffraction (XRD) measurements were carried out on the Bruker D8 Discover device using Cu Kα radiation (λ=1.54 Å) as the X-ray source. The device voltage and applied current were 40 kV and 40 mA, respectively. Crystallite sizes (D, nm) were calculated using the Scherrer equation (Eq. (1)) regarding the reflection related to the (1 0 1) plane of ZnO.

$$D = K\lambda / (\beta \cos\theta) \quad (1)$$

where K = 0.9, λ is the X-ray wavelength (1.5418 Å), θ is the Bragg angle, and β is the full width at half maximum intensity (FWHM, radians) [29].

Scanning electron microscopy (SEM) analysis was carried out on an FEI-Philips XL30 SEM-EDAX operating at an accelataring voltage of under 10 kV. Photoluminescence (PL) features were investigated using a fluorescence spectrometer (Edinburgh Instruments Spectrofluorometer FS5). A PerkinElmer STA 600 model device was employed for the thermogravimetric analysis (TGA), which was conducted at temperatures ranging from 30 to 800 °C in a nitrogen environment (20 mL/min). Brunauer-Emmett-Teller (BET) surface areas and Barrett-Joyner-Halenda (BJH) pore size distributions of the filters and photocatalysts were determined using a Quantachrome Quadrosorb SI device with nitrogen adsorption at 77 K.

2.4. Photocatalytic activity experiments

Photocatalytic activity experiments under UV-A light were carried

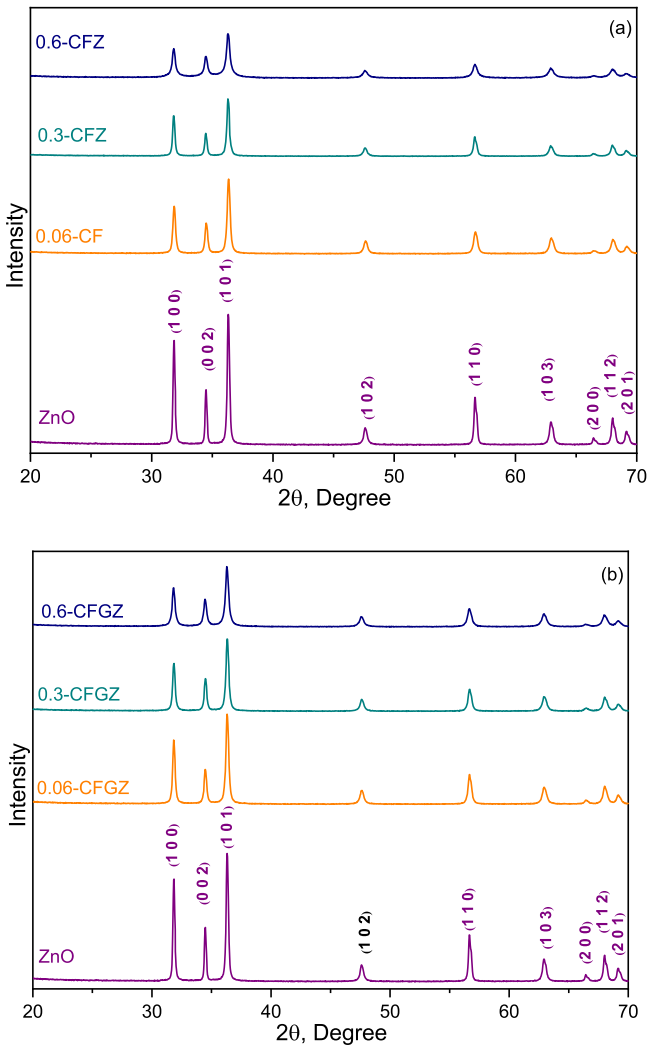

Fig. 6. XRD diffractograms of (a) ZnO particles and CFZ photocatalysts, (b) ZnO particles and CFGZ photocatalysts.

out in a specially designed system comprising a cylindrical Pyrex reactor vessel placed on a magnetic stirrer and illuminated from above with a 125 W black fluorescent lamp (BLF). The BLF light source was in the range of 300 to 420 nm, with a maximum emission at 365 nm. Photocatalytic experiments were performed in a 50 mL pyrex reaction vessel at room temperature (25 °C ± 2 °C) and natural pH. The optimum amount of photocatalyst was 0.25 mg/mL and the MB dye concentration was 5 mg/L. At certain time intervals (t = 0, 30, 60, 90, 120, 150, 210, and 270 min), samples were collected from the reaction vessel and filtered through a 0.22 μm Millipore acetate membrane filter. The absorbance of the filtered MB solutions was measured at 246 nm, 292 nm, and 664 nm by a UV–vis spectrophotometer (Shimadzu UV-2600). The reproducibility of the results was determined as <5 % via preliminary experiments performed in triplicate prior to the main experimental part.

3. Results and discussion

3.1. Characterization of CF and CFG

FTIR spectroscopy was used to determine the presence of the functional groups in both CF and CFG specimens (Fig. 1(a)). A wide peak in the FTIR spectrum of the CF centered at around 3492 cm^{-1} was attributed to the -OH stretching vibration, resulting from the absorbed water molecules. The two peaks observed at 2925 cm^{-1} and 2853 cm^{-1} were identified as the symmetrical and asymmetrical C—H stretching vibrations in the methyl group, respectively. The peaks at 1736 cm^{-1}, 1431 cm^{-1}, 1367 cm^{-1}, and 1216 cm^{-1} were related to the C = O stretching vibration of the acetate groups, -CH_2 bending, -CH group bending, and C—O bond stretch in acetyl groups, respectively. The peaks at 1125 cm^{-1} and 1032 cm^{-1} corresponded to the asymmetrical C—O-C stretching in the ester group and the vibrational mode of the C—O bond in cellulose molecules, respectively [30]. Furthermore, the peaks at 899 cm^{-1} and 602 cm^{-1} were attributed to the glycosidic unit of cellulose acetate and the C—H stretching in the acetyl group, respectively [27,31]. As anticipated, the peak intensities and positions in the FTIR spectrum of CFG remained unaltered.

The XRD diffractograms of the CF and CFG specimens exhibited a single broad characteristic band in the range of 2θ=10–30° centered at around 2θ=14° (Fig. 1(b)). This band indicated the presence of an amorphous structure [32].

SEM images of CF exhibited smooth, long filamentous strips that terminate in a triangular cross-sectional form [33]. A slight deformation was observed during the grinding process as evidenced by the SEM images of CFG (Fig. 2).

The elemental compositions of the CF and CFG specimens, as determined by EDAX spectra, are presented in the Supplementary Material (SM), Part I, Figure SM1. The EDAX data consisted mainly of carbon and oxygen, with trace amounts of titanium and aluminum. The principal usage of titanium in CFs is to give a white color and it's also well known that nanomaterials containing titanium are used to reduce the harmful chemicals inhaled by smokers [30,34]. The presence of heavy metals on the other hand, can be ascribed to various factors including the cultivation of tobacco, soil contamination, the cigarette manufacturing process, and the use of brightening agents on paper [30, 34].

Thermogravimetric data for CFG were presented as a TG curve and a derivative thermogravimetric DTG in Fig. 3. The initial stage of the mass loss was due to the dehydration, with a loss of 10 % observed up to around 205 °C. The second stage was the plasticizer used in filter making and this degradation step was found to correspond to the deacetylation process of cigarette filters [30]. As the temperature of 394 °C was reached, a mass loss of 84 % was observed. Therefore, it can be concluded that a burning temperature above 400 °C is sufficient to remove the CFG template and obtain C-ZnO photocatalysts.

Nitrogen adsorption-desorption isotherms and the corresponding BJH pore-size distribution curves of CF and CFG specimens are displayed in Fig. 4. CF and CFG specimens exhibited Type IV isotherms according to the IUPAC classification that was characteristic of mesoporous materials [35]. The BET-specific surface areas (S_{BET}) of CF and CFG were 26 m^2/g and 50 m^2/g, respectively, and the grinding process resulted in an almost doubled surface area. The differences between the specimens could be attributed to the morphological changes already observed in the SEM images (Fig. 2). The pore diameters of CF and CFG were approximately 3 nm and 2 nm, respectively.

3.2. Characterization of photocatalysts

3.2.1. FTIR analysis

FTIR analysis was carried out to ascertain the possible differences in functional groups of the CFZ, CFGZ, and ZnO specimens, and related FTIR spectra were presented in Fig. 5.

A wide peak centered at approximately 3429 cm^{-1} in the FTIR spectrum of ZnO belonged to the -OH stretching vibration of water molecules (Figure 5(a), (b)). The peaks at 1637 cm^{-1}, and 1395 cm^{-1}, corresponded to the H–O–H bending and trace amounts of nitrate ions from the precursor, respectively. The peaks located in the 920–500 cm^{-1} low-frequency region corresponded to Zn–O–Zn and Zn–O stretching vibrations [16,36–38]. The peaks observed at 3506 cm^{-1}, 2988 cm^{-1}, 2902 cm^{-1}, and 1523 cm^{-1} corresponded to the -OH stretching,

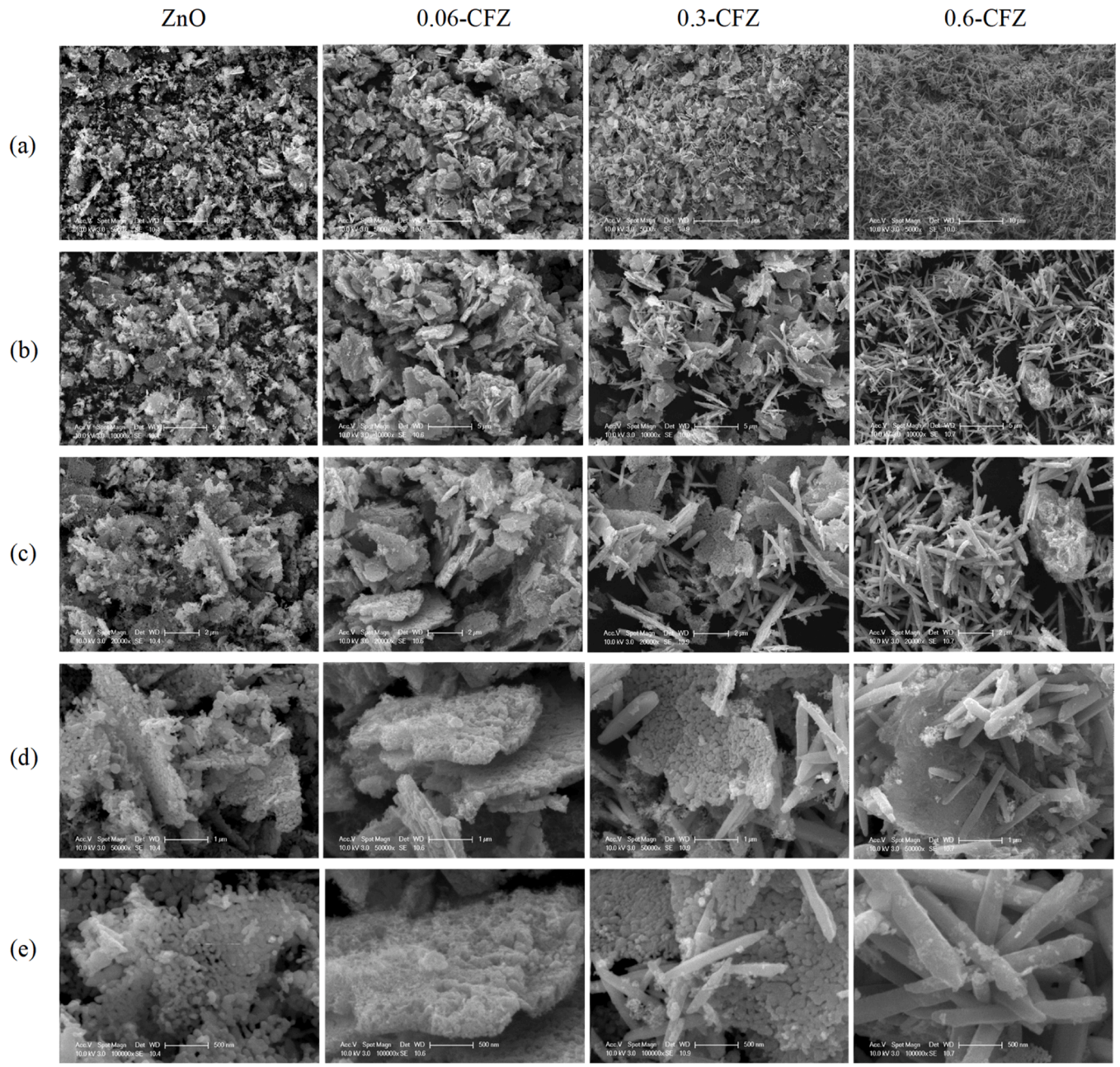

Fig. 7. SEM images of ZnO particles and CFZ specimens at different magnifications (a) 5000x, (b) 10000x, (c) 20000x, (d) 50000x, (e) 100000x.

symmetrical and asymmetrical C—H stretching in the methyl group, and H–O–H bending, respectively (Fig. 5(a)) [16,30,39]. The peak at 1394 cm^{-1} indicated the presence of nitrate ions [38]. The peaks at 1077 cm^{-1} and 1047 cm^{-1} were Zn-O-Zn asymmetric stretching vibrations of the oxygen bridge in the orthorhombic structure [40]. The peaks located in the 880–500 cm^{-1} region belonged to the Zn-O stretching vibration [41]. The absence of characteristic intense acetate peaks at 1736 cm^{-1} and 1216 cm^{-1} related to the C═O stretching and C—O bond stretching vibrations, indicated the removal of the CF template after the calcination [30]. A slight shift was observed for 0.3-CF and 0.06-CF specimens. All CFGZ specimens exhibited similar spectra regarding the position of characteristic peaks, shape, and size with only a slight change indicating that mechanical grinding did not affect the functional groups of the photocatalysts. (Fig. 5(b)).

3.2.2. Raman analysis

Raman spectra are given in SM, Part II, Figure SM2. The intense band at 435 cm^{-1} in the Raman spectrum of ZnO corresponded to the E_2 (high) vibration mode. The other bands observed at 321 cm^{-1}, 381 cm^{-1}, 585 cm^{-1}, 680 cm^{-1}, and 1161 cm^{-1} were assigned to the $2E_2$ mode, A_1 (TO) mode, A_1 (LO) mode, TA+LO, $2A_1$ (LO) contributions, and $2E_1$ (LO) modes, respectively [15]. The Raman spectrum of 0.06-CFG revealed bands at 437 cm^{-1}, 330 cm^{-1}, and 383 cm^{-1} attributed to E_2 (high), $2E_2$ mode, and A_1 (TO) modes of ZnO. In the Raman spectrum of 0.6-CFG, the intensity of the prominent band related to the E_2 (high) mode of ZnO shifted to a lower wavenumber (428 cm^{-1}), and the intensity also decreased (Figure SM2 (a)). Furthermore, the peak of the oxygen vacancy A_1 (TO) mode at ZnO (382 cm^{-1}) was shifted remarkably compared to CFZ specimens, indicating the carbon self-doping process [42]. Same kind of changes in the Raman spectra of CFGZ were noted (Figure SM2 (b)).

3.2.3. XRD analysis

XRD diffractograms of ZnO, CFZ, and CFGZ specimens are shown in

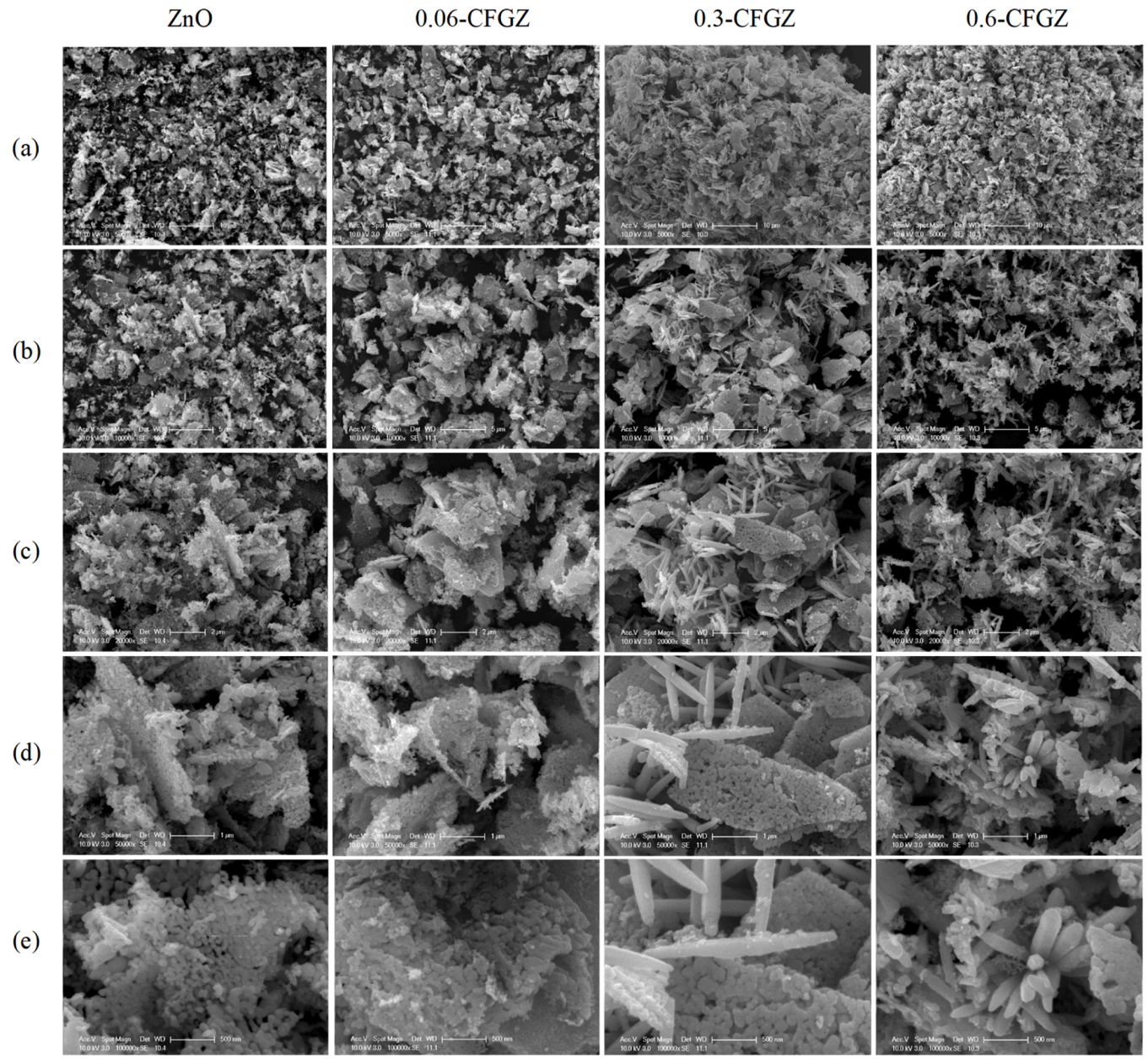

Fig. 8. SEM images of ZnO particles and CFGZ specimens at different magnifications (a) 5000x, (b) 10000x, (c) 20000x, (d) 50000x, (e) 100000x.

Fig. 6. For ZnO, the diffraction peaks located at 2θ=31.86°, 34.50°, 36.34°, 47.64°, 56.70°, 62.95°, 66.43°, 68.04°, and 69.19° corresponded to the (1 0 0), (0 0 2), (1 0 1), (1 0 2), (1 1 0), (1 0 3), (2 0 0), (1 1 2), and (2 0 1) planes of ZnO, respectively. All peaks were consistent with zincite hexagonal ZnO structure (JCPDF 36–1451). In the case of 0.06-CFZ, the diffraction peaks at 2θ=31.82°, 34.47°, 36.30°, 47.59°, 56.65°, 62.91°, and 68.00° were assigned to the (1 0 0), (0 0 2), (1 0 1), (1 0 2), (1 1 0), (1 0 3), and (1 1 2) planes of ZnO, respectively, whereas the diffraction planes of (2 0 0) and (2 0 1) disappeared (Fig. 6(a)). Besides, the peaks shifted slightly toward the lower angles in CFZ specimens which could be due to the substitution of the oxygen atom in the ZnO matrix by carbon [43]. In addition, the absence of an impurity phase indicated that carbon successfully entered the ZnO crystal lattice [42]. Furthermore, the intensity of the peaks gradually decreased, and the width of the diffraction peaks enlarged gradually as the CF amount increased in CFZ and CFGZ specimens (Fig. 6). The data implied that the possible inhibition role of carbon on the growth of ZnO results in a downward trend in the crystalline quality of ZnO with the increase of carbon self-doping [42,43]. The results of XRD were in good agreement with the Raman data.

The calculated crystallite sizes of the specimens using the Scherrer equation from the ZnO (1 0 1) diffraction peak were listed in SM, Part II, Table SM1. A gradual increase in size was observed as the carbon quantity in photocatalysts increased due to the burning of the template. The reason could be the formation of oxygen defects resulting in the expansion of the crystal lattice [42].

3.2.4. *SEM analysis*

SEM analysis was performed to determine the morphological changes and sizes of ZnO, CFZ, and CFGZ specimens with five different magnifications (Figs. 7 and 8). SEM image of ZnO consisted of irregular polyhedral-shaped particles with a slight agglomeration. Compared to ZnO, a rougher surface was found in the 0.06-CFZ (Fig. 7) due to the origin of the CF template presented in Fig. 2. It was noted that the original shape and morphology of ZnO specimen were almost maintained after the CF addition in the 0.06-CFZ specimen. However, the

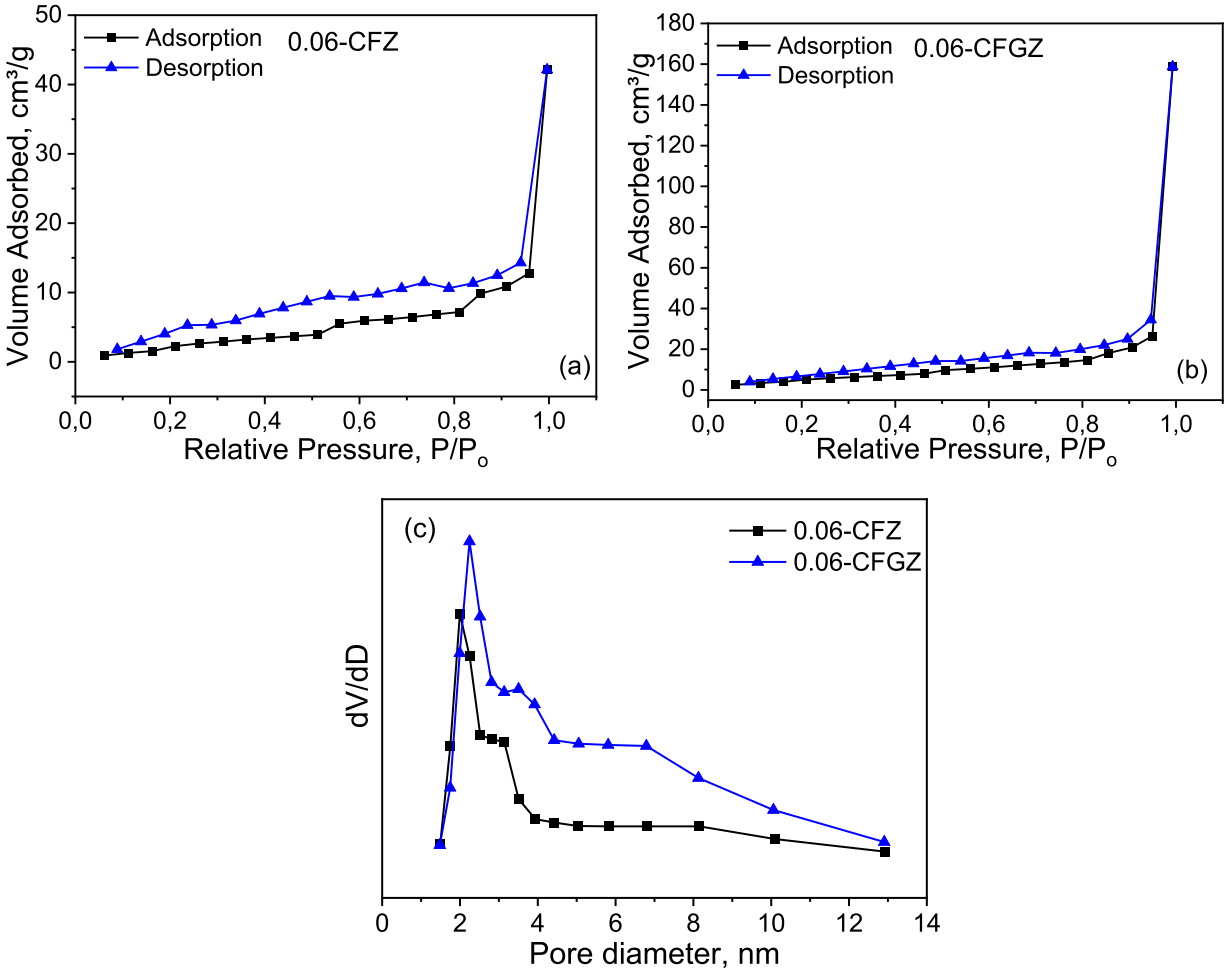

Fig. 9. Nitrogen adsorption-desorption isotherms of (a) 0.06-CFZ, (b) 0.06-CFGZ, and (c) pore size distribution plots of 0.06-CFZ and 0.06-CFGZ.

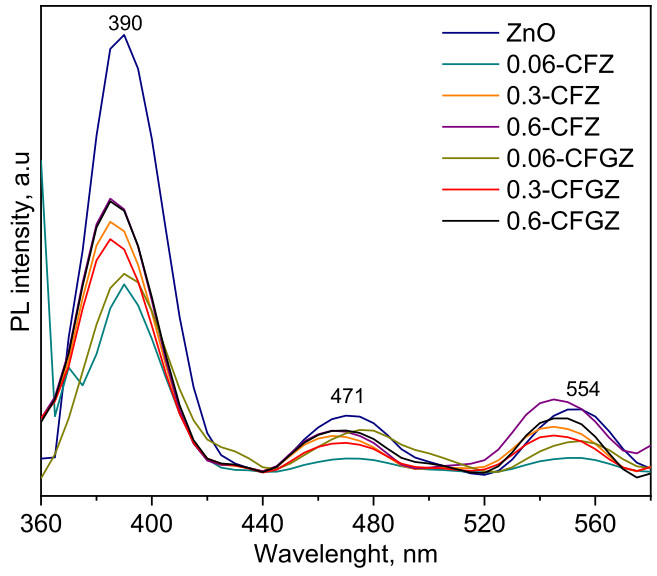

Fig. 10. Photoluminescence spectra of ZnO, CFZ, and CFGZ specimens.

SEM image of 0.3-CFZ was similar to the morphologies of both ZnO and CF containing mainly protected forms of irregularly shaped ZnO particles and the presence of covered CF-shaped ZnO particles, resulting in a slightly larger particle size than ZnO. In the case of loading a higher amount of CF, a well-ordered continuous coating layer of ZnO along CF was observed especially in the images at higher magnifications (50000x and 100000x), and this also caused a change in the dominant morphology of the 0.6-CFZ specimen.

CFGZ photocatalysts demonstrated a similar distribution in the morphological trend with less agglomeration throughout the CF concentration (Fig. 8). A tendency of ZnO-shaped particle morphology could be observed on the surface of the base 0.06-CFGZ, while further increasing the CFG amount, 0.3-CFGZ specimen revealed more template-shaped formed morphology. ZnO morphology transformed from irregular polyhedral-shaped particles to the sacrificial CFGZ template morphology in the 0.6-CFGZ specimen. The grinding process of the template slightly improved the uniformity and porosity of CFGZ specimens.

The EDAX spectra of ZnO, CFZ, and CFGZ specimens were presented in SM, Part II, Figure SM3. The elemental analysis of ZnO nanoparticles confirmed the presence of zinc and oxygen element signals. The EDAX spectra of CFZ and CFGZ specimens presented carbon and traces of titanium (< 1 %) elements derived from a sacrificial template while zinc and oxygen came from as-synthesized ZnO. C-ZnO specimens tended to reveal an increasing order of carbon amount with increasing template loading.

3.2.5. *BET analysis*

BET Nitrogen adsorption-desorption isotherms of 0.06-CFZ and 0.06-CFGZ photocatalysts are given in Fig. 9 where the graphs showcase type IV isotherm with a H3 hysteresis loop at high relative pressure (P/P_0 >0.8) characteristics as classified by IUPAC [35]. Type IV isotherm

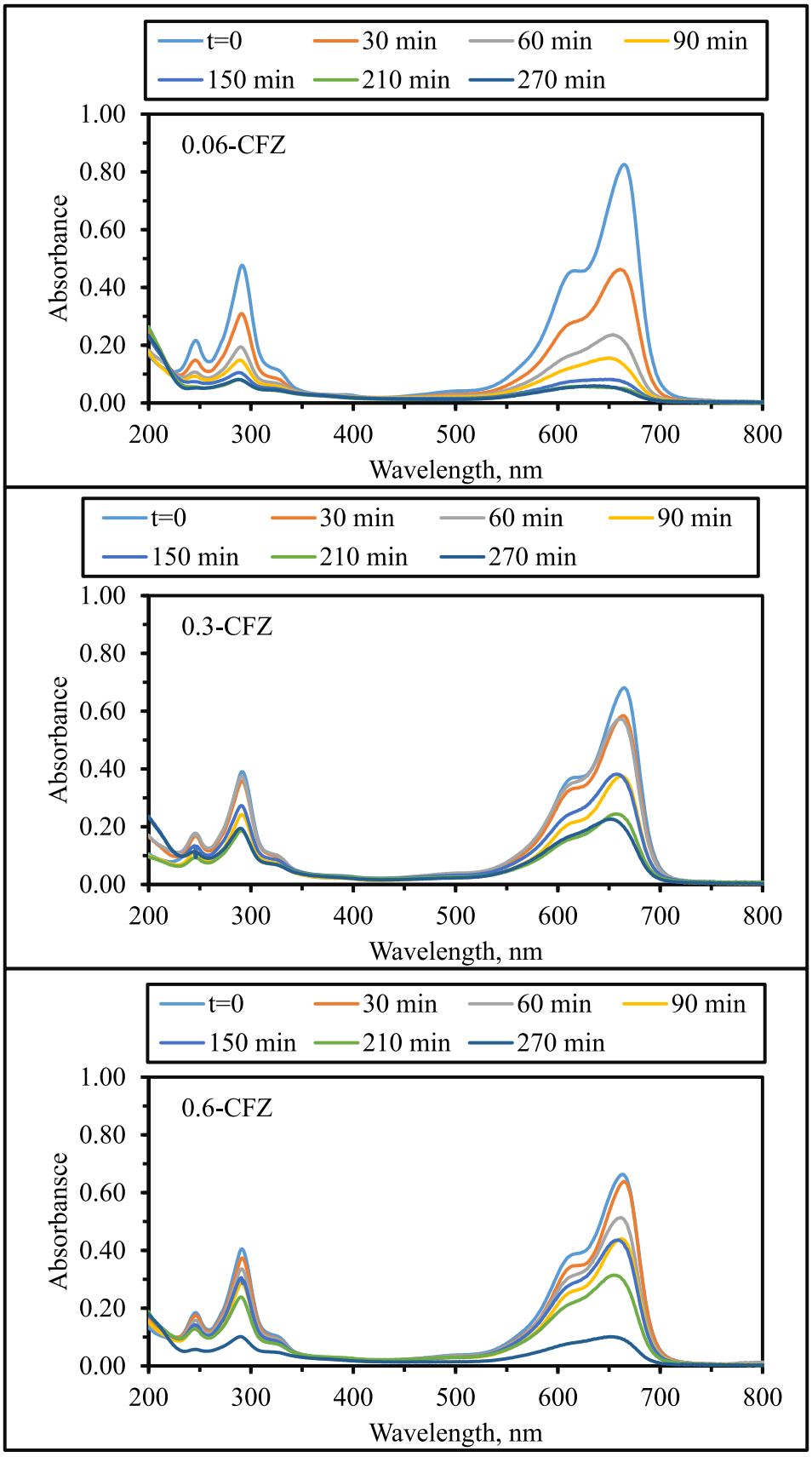

Fig. 11. UV–vis absorption spectra of MB using CFZ photocatalysts.

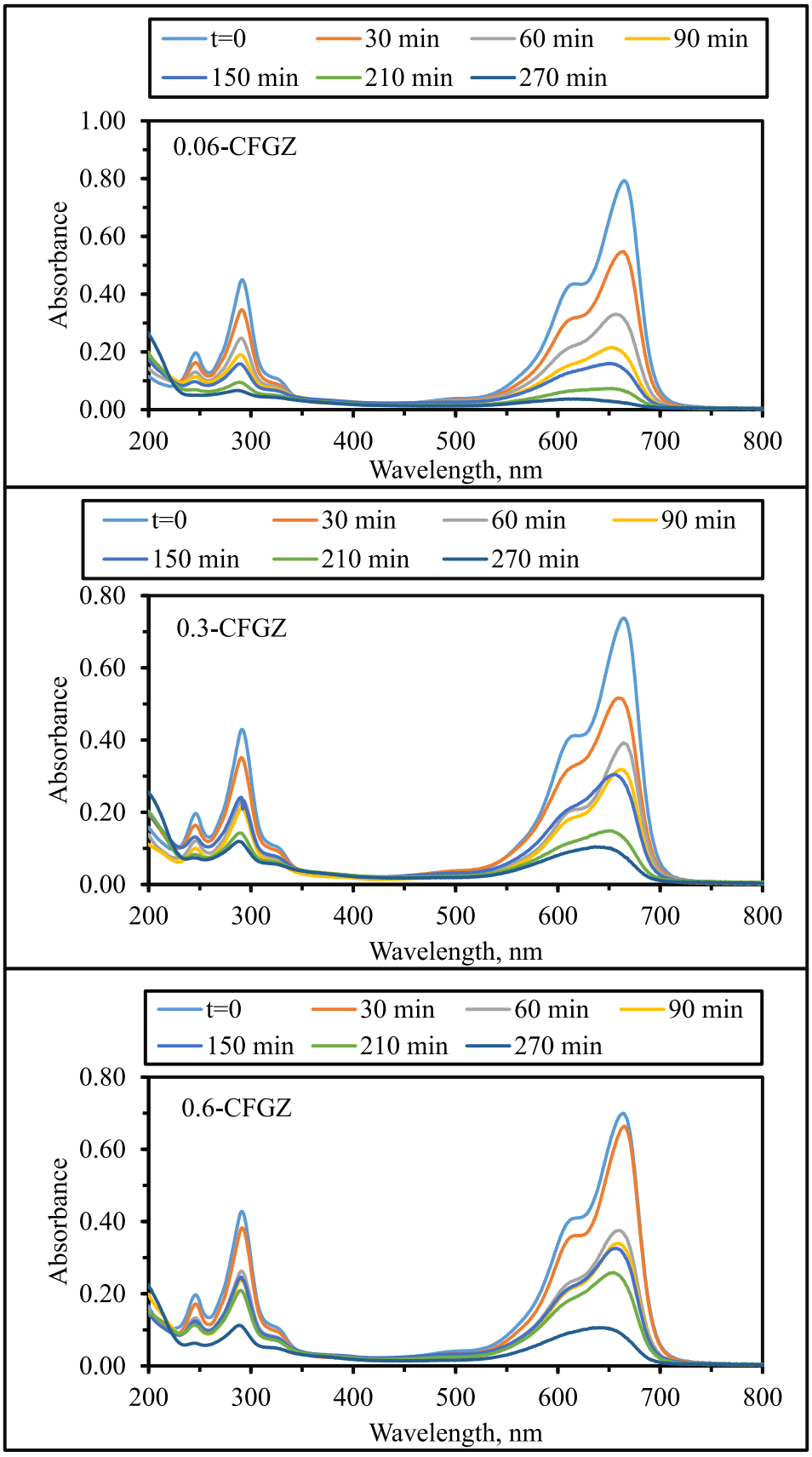

Fig. 12. UV–vis absorption spectra of MB using CFGZ photocatalysts.

Table 1
Photocatalytic degradation kinetics of MB expressed by A_{664}, A_{292}, and A_{246}.

First Order Kinetic Parameters			
A_{664}	$k \times 10^{-3}$, min^{-1}	$t_{1/2}$, min	Rate, cm^{-1} min^{-1}
0.06-CFZ	11.0	63	0.0106
0.3-CFZ	5.32	130	0.0051
0.6-CFZ	7.03	99	0.0068
0.06-CFGZ	12.7	55	0.0122
0.3-CFGZ	8.26	84	0.0079
0.6-CFGZ	7.44	93	0.0072
A_{292}			
0.06-CFZ	6.87	101	0.0037
0.3-CFZ	3.61	192	0.0020
0.6-CFZ	4.95	140	0.0027
0.06-CFGZ	7.39	94	0.0040
0.3-CFGZ	5.07	137	0.0028
0.6-CFGZ	4.77	145	0.0026
A_{246}			
0.06-CFZ	6.07	114	0.0015
0.3-CFZ	3.64	190	0.0009
0.6-CFZ	4.85	143	0.0012
0.06-CFGZ	6.14	113	0.0015
0.3-CFGZ	4.37	157	0.0011
0.6-CFGZ	4.59	151	0.0011

yielded a typical type of monolayer and multilayer nitrogen adsorption while the H3 hysteresis loop confirmed the aggregation of plate-like particles into slit-shaped pores [44]. The specific surface areas of 0.06-CFZ and 0.06-CFGZ were 10 m^2/g and 23 m^2/g, respectively, indicating that the grinding process doubled the surface area. Based on the results given in Fig. 9(c), the average pore diameters of 0.06-CFZ and 0.06-CFGZ were 2.1 nm and 2.2 nm, respectively, falling in the mesoporous classification (2–50 nm) [35]. The pore volumes were 0.069 mL/g and 0.252 mL/g, respectively. The observed increased agglomeration in 0.06-CFZ compared to 0.06-CFGZ could lead to blocking the pores on an internal surface of the particle in agreement with SEM data (Figs. 7 and 8) [45].

3.2.6. Photoluminescence analysis

PL analysis was carried out to assess the recombination rate of charge carriers in ZnO particles and CFZ and CFGZ specimens (Fig. 10). The ZnO spectrum consisted of a strong UV emission band at λ=390 nm (3.18 eV), a blue-green band at λ=471 nm (2.63 eV), and a green band at λ=554 nm (2.24 eV). The intense UV emission band could belong to the exciton recombination-related near-band edge emission of ZnO while the blue-green and green emission bands could be attributed to the surface defect and the singly ionized oxygen vacancy in ZnO, respectively [15,46]. These three characteristic emission bands of ZnO were also observed in the PL spectra of CFZ and CFGZ specimens with a significant decrease in PL intensity. The reduction in emission intensity could confirm an electronic interaction between carbon and ZnO due to the self-carbon doping of ZnO. This finding was well in accordance with the result of EDAX. It was also previously reported that a low PL intensity indicated a decrease in the recombination of electron/hole pairs on the semiconductor surface [47].

Upon loading a low-carbon template source for 0.06-CFZ and 0.06-CFGZ specimens, self-carbon doping could act as electron trappers to separate the electron-hole pairs. However, a high carbon source could be an excessive dopant amount that possibly performed as a recombination center for the photoinduced electron/hole pairs [43]. Among the synthesized CFZ and CFGZ specimens, the lowest intensity was observed with 0.06-CFZ signifying an efficient charge transfer resulting in reduced electron/hole recombination and improved photocatalytic activity. However, several factors such as particle size, recombination velocity, and defects could affect PL spectra. Hence, it was not possible to make an evaluation arising from the PL due to the complex mechanism of a semiconductor [44].

3.3. Photocatalytic activity experiments

Photocatalytic activities of CFZ and CFGZ were characterized based on their interactions with MB under irradiation. The decolorization efficiencies were shown by UV–vis spectral analysis, experimental parameters as well as kinetic modeling.

3.3.1. Photocatalytic degradation of MB using CFZ and CFGZ photocatalysts

The variations over time (0–270 min) in the UV–vis absorbance spectra of the MB solution (5 mg/L) after treatment with CFZ, and CFGZ specimens (0.25 g/L) were presented in Figs. 11 and 12. UV–vis spectrum and molecular structure of MB are given in SM, Part III, Figure SM4.

The UV–vis absorption spectrum of MB mainly consisted of a peak with a shoulder at 664 nm and 617 nm, respectively, related to the auxo chromic group of dye. The main peak at 664 nm belonged to a long conjugation system that occurred in the range 550–700 nm between two dimethylamine-substituted aromatic rings through the sulfur and nitrogen, where the observed shoulder at 617 nm was responsible for the absorbance of the MB dimer. The two spectral peaks in the UV region at λ=246 nm and λ=292 nm correspond to the substituted benzene ring structure [48,49].

The characteristic absorption peaks of MB at λ=246 nm, λ=292 nm, and λ=664 nm were chosen for monitoring the photocatalytic degradation process induced by CFZ and CFGZ specimens. During the photocatalytic degradation, intensities of three absorbance reduced gradually with the increase of reaction time. The reduction of the peak intensities correspond to MB degradation, followed by generated smaller intermediates that could successfully be degraded during the photocatalytic degradation process. The reason could be the formation of main aromatic sub-group intermediates such as demethylated metabolites, sulfoxide, sulfonic acid, and phenolic compounds. This phenomenon could also be supported in that the absorption peaks of these compounds were also observed at wavelengths in the region of λ=200–300 nm and λ=500–700 nm overlapping the absorption spectra of MB. For this reason, it was difficult to identify the intermediates [49].

3.3.2. Kinetics of photocatalytic degradation

All UV–vis parameters displayed logarithmic decay profiles as presented in SM, Part III, Figures SM5 following pseudo-first-order kinetic model expressed by Eq. (2):

$$\text{Rate}(R) = -dA/dt = kA \quad (2)$$

where,

R: pseudo-first-order rate ($cm^{-1}min^{-1}$),

A_o: initial absorbance of MB expressed as $A_{664,o}$, $A_{292,o}$ and $A_{246,o}$,

A: absorbance of MB expressed as A_{664}, A_{292} and A_{246} at time t, t: irradiation time, min, k: pseudo-first-order reaction rate constant, min^{-1}.

Half-life ($t_{1/2}$, min) could easily be calculated by the following equation, $t_{1/2} = 0.692/k$.

Kinetic model parameters ($R^2 > 0.85$) are listed in Table 1. The highest decolorization rate constant was achieved with 0.06-CFZ and 0.06 CFGZ photocatalysts, respectively. The degradation rate constants of MB (A_{664}) were calculated as $k = 11.0 \times 10^{-3}$ min^{-1} and $k = 12.7 \times 10^{-3}$ min^{-1} for 0.06-CFZ and 0.06 CFGZ photocatalysts, respectively. These values were almost two times the decolorization rate constant of MB obtained in the presence of 0.3-CFZ (5.32×10^{-3} min^{-1}). This can be attributed to the role of carbon amount and zinc-oxygen defects reducing the recombination rate of electron-hole pairs, as confirmed by PL spectra (Fig. 10) [50,51].

Degradation of aromatic groups yielded rate constants as $k = 6.87 \times 10^{-3}$ min^{-1} and 6.07×10^{-3} min^{-1} for A_{292} and A_{246} in the presence of 0.06-CFZ photocatalyst, respectively. Upon the use of 0.06-CFGZ, the

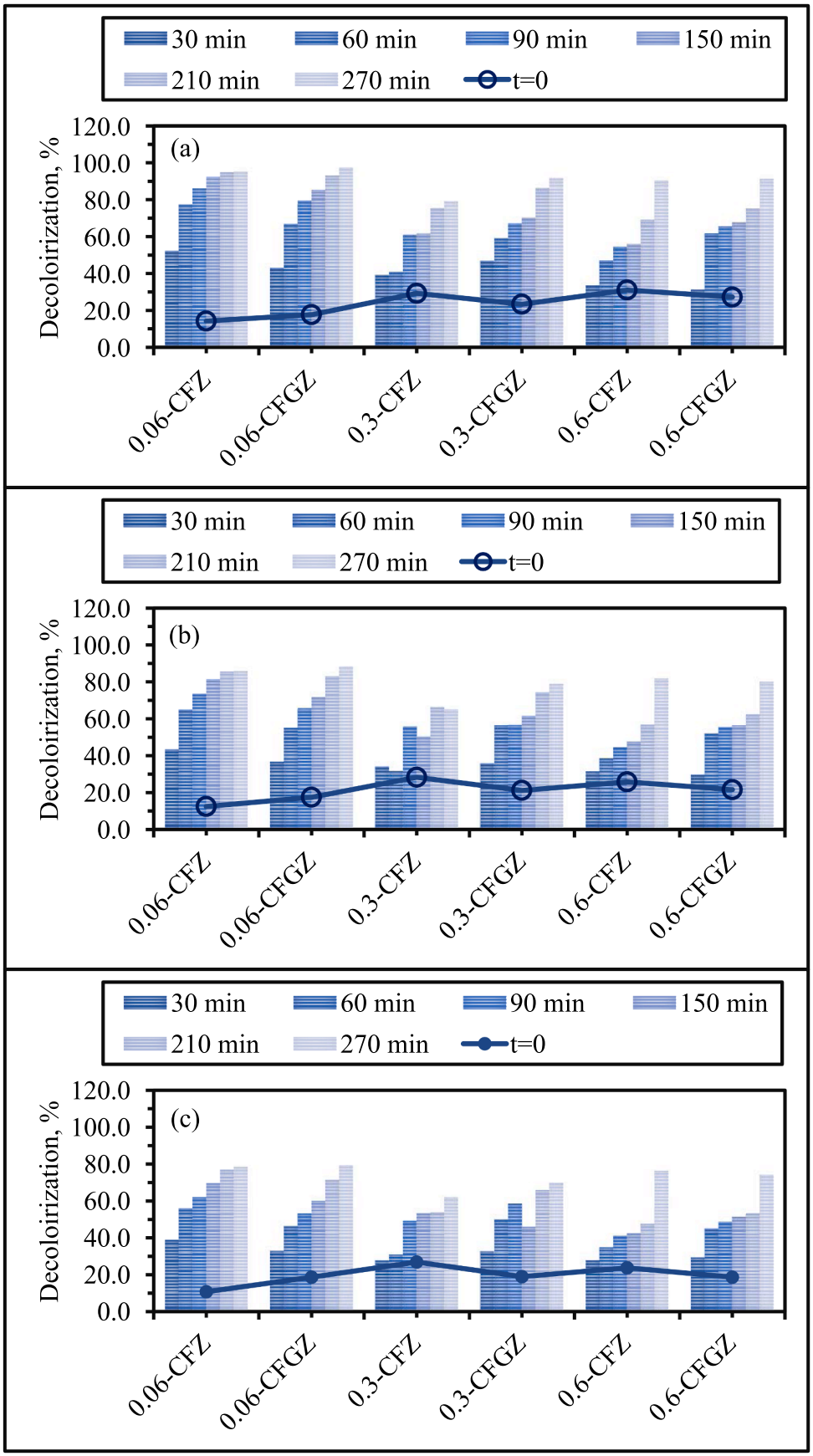

Fig. 13. Photocatalytic degradation of MB for (a) A_{664}, (b) A_{292}, and (c) A_{246} upon use of CFZ and CFGZ photocatalysts.

calculated rate values were slightly higher than 0.06-CFZ specimen and revealed as $k = 7.39 \times 10^{-3}$ min^{-1} and 6.14×10^{-3} min^{-1}.

CFGZ specimens exhibited better photocatalytic activity compared to the photocatalyst series of CFZ. The reason could be explained by the SEM images of CFGZ specimens (Fig. 8) that presented fewer aggregated particles than CFZ specimens (Fig. 7). 0.06 CFGZ photocatalyst exhibited the highest photocatalytic activity among all specimens which could be attributed to the almost uniform morphology (Fig. 8) with a large surface area (23 m^2/g). A higher surface area could provide more reactive sites, improving photocatalytic degradation efficiency since photocatalytic reactions mostly occur on the photocatalyst surface [52].

According to values obtained from Table 1, the trend in photocatalytic degradation rate constants in the presence of all photocatalysts could be given in decreasing order:

A_{664}: 0.06-CFGZ > 0.06-CFZ > 0.3-CFGZ > 0.6-CFGZ > 0.6-CFZ > 0.3-CFZ.

A_{292}: 0.06-CFGZ > 0.06-CFZ > 0.3-CFGZ > 0.6-CFZ > 0.6-CFGZ > 0.3-CFZ.

A_{246}: 0.06-CFGZ > 0.06-CFZ > 0.6-CFZ > 0.6-CFGZ > 0.3-CFGZ > 0.3-CFZ.

The trend was the same as that of 0.06-CFGZ and 0.06-CFZ specimens for the rate constants of A_{292} and A_{246}.

The degree of MB decolorization by using CFGZ and CFZ specimens (Fig. 13) was also calculated by the following Eq. (3-5):

$$\text{Decolorization}, \% = \left(\left(A_{664,o} - A_{664}\right) / A_{664,o}\right)\right) \times 100 \quad (3)$$

$$\text{Decolorization}, \% = \left(\left(A_{292,o} - A_{292}\right) / A_{292,o}\right)\right) \times 100 \quad (4)$$

$$\text{Decolorization}, \% = \left(\left(A_{246,o} - A_{246}\right) / A_{246,o}\right)\right) \times 100 \quad (5)$$

where,

$A_{664,o}$, $A_{292,o}$ and $A_{246,o}$ were the initial absorbance of MB

A_{664}, A_{292}, and A_{246} were the absorbance of MB at time t.

Accordingly, the initial surface coverage extents ($t = 0$) of A_{664} for 0.06-CFZ and 0.06 CFGZ specimens were 14 % and 18 %, respectively. These values increased for the photocatalysts containing higher amounts of CF and CFG possibly due to the enhancement of surface area concerning the amount of substrate. From a general perspective, CFZ and CFGZ specimens followed a similar trend as A_{292} and A_{246}. However, the extent of the surface exhibited an inconsistent trend for both the preparation method and CF and CFG amounts. Since the adsorption capacity was included within surface phenomena, this result was consistent with the BET-specific surface area data and was 10 m^2/g and 23 m^2/g for 0.06-CFZ and 0.06-CFGZ specimens, respectively.

Decolorization percentage values of MB achieved by using CFZ and CFGZ photocatalysts were listed in SI Part III, Table SM2. Upon using 0.06-CFZ and 0.06-CFGZ specimens, almost a complete decolorization of MB was achieved following a prolonged period of up to 270 min. Moreover, the decolorization percentage of MB in the presence of both 0.3-CFGZ and 0.6-CFGZ specimens revealed the lowest performance. The reason could be ascribed to the observed tendency of agglomeration in catalysts containing a higher amount of CF and CFG (Figs. 7 and 8). Upon irradiation during photocatalysis, a similar trend was observed with the UV–vis spectral features (A_{292} and A_{264}) expressing the degradation of aromatic groups of MB. In addition, it should be stated that the focus of this study was directed to the preparation of the carbon self-doped ZnO photocatalysts using two different templates rather than concentrating on the degradation pathways of MB under the specified experimental conditions.

4. Conclusions

The purpose of the study was to develop cost-effective C-ZnO photocatalysts via a facile one-step precipitation method using CF and CFG as carbon sources and templates. A mechanical process based on grinding and sieving did not impact the surface functional groups and structure of CF and CFG. However, the grinding process influenced the morphological characteristics of a long strip structure and triangular cross-section of CF and doubled the surface area. FTIR confirmed the functional groups of ZnO and the presence of CF/CFG as the carbon source. The addition of CF/CFG as templates played a key role in the morphological characteristics and crystallite sizes of C-ZnO photocatalysts. The high amounts of CF/CFG increased particle aggregation, particularly in 0.6-CFZ and 0.6-CFGZ specimens, and exhibited specific dominant morphology in the sacrificial templated forms. The photocatalytic activities of C-ZnO photocatalysts were evaluated by monitoring the degradation of MB dye. The photocatalytic degradation rate constants of MB (A_{664}) were calculated as $k = 11.0 \times 10^{-3}$ min^{-1} and $k = 12.7 \times 10^{-3}$ min^{-1} for 0.06-CFZ and 0.06 CFGZ photocatalysts, respectively. The photocatalytic degradation of MB showed a correlation between template amount and morphology of C-ZnO specimens. Amongst all photocatalysts, 0.06-CFGZ specimen exhibited maximum photocatalytic efficiency that could be explained based on its unique template-based morphology, mesoporous nature, and high surface area. Furthermore, the high efficiency of this photocatalyst could also be due to the reduced electron/hole recombination as shown by PL spectra. The finding suggested the potential of using cigarettes or environmental solid waste CF as a carbon source and template for preparing doped C-ZnO photocatalysts via a facile one-step method to address wastewater treatment issues. As future work, we plan to conduct a comparative study on the photocatalytic performance under both UV and visible light conditions to fully elucidate the benefits of carbon doping and the full potential of the newly synthesized photocatalysts.

CRediT authorship contribution statement

Yasemin Aytac: Investigation, Formal analysis. **Nazli Turkten:** Writing – review & editing, Conceptualization. **Dila Kaya:** Writing – review & editing, Writing – original draft, Supervision, Conceptualization.

Declaration of competing interest

The authors declare that they have no known competing financial interests or personal relationships that could have appeared to influence the work reported in this paper.

Acknowledgments

This research did not receive any specific grant from funding agencies in the public, commercial, or not-for-profit sectors.

Supplementary materials

Supplementary material associated with this article can be found, in the online version, at doi:10.1016/j.molstruc.2025.141764.

Data availability

Data will be made available on request.

References

[1] M. MuthuKathija, S. Muthusamy, R. Imran Khan, M. Sheik Muhideen Badhusha, K. Rajalakshmi, V. Rama, Y. Xu, Photocatalytic degradation of methylene blue dye using biogenic copper oxide nanoparticles and its degradation pathway analysis, Inorg. Chem. Commun. 161 (2024) 111929.

[2] A. Panda, P.P. Samal, M.A. Qaiyum, B. Dey, S. Dey, Think before throw: waste chili stalk powder for facile scavenging of cationic dyes from water, Environ. Monit. Assess. 196 (2) (2024) 118.

[3] M.N. Pervez, M.M. Hassan, V. Naddeo, Separation of cationic methylene blue dye from its aqueous solution by S-sulfonated wool keratin-based sustainable

electrospun nanofibrous membrane biosorbent, Sep. Purif. Technol. 333 (2024) 125903.
[4] L. Baloo, M.H. Isa, N.B. Sapari, A.H. Jagaba, L.J. Wei, S. Yavari, R. Razali, R. Vasu, Adsorptive removal of methylene blue and acid orange 10 dyes from aqueous solutions using oil palm wastes-derived activated carbons, Alex. Eng. J. 60 (6) (2021) 5611–5629.
[5] H.N. Hamad, S. Idrus, Recent developments in the application of bio-waste-derived adsorbents for the removal of methylene blue from wastewater: a review, Polymers. (Basel) 14 (4) (2022) 783.
[6] Y.N. Teixeira, F.J. de Paula Filho, V.P. Bacurau, J.M.C. Menezes, A. Zhong Fan, R.P. F. Melo, Removal of methylene blue from a synthetic effluent by ionic flocculation, Heliyon. 8 (10) (2022) e10868.
[7] Q. Li, Y. Li, X. Ma, Q. Du, K. Sui, D. Wang, C. Wang, H. Li, Y. Xia, Filtration and adsorption properties of porous calcium alginate membrane for methylene blue removal from water, Chem. Eng. J. 316 (2017) 623–630.
[8] R.M. Reema, P. Saravanan, M.D. Kumar, S. Renganathan, Accumulation of methylene blue dye by growing Lemna minor, Sep. Sci. Technol. 46 (6) (2011) 1052–1058.
[9] S.Y. Kim, I.Y. Kim, S.-H. Park, M. Hwangbo, S. Hwangbo, Novel ultrasonic technology for advanced oxidation processes of water treatment, RSC. Adv. 14 (17) (2024) 11939–11948.
[10] Z. Masood, A. Ikhlaq, A. Akram, U.Y. Qazi, O.S. Rizvi, R. Javaid, A. Alazmi, M. Madkour, F. Qi, Application of nanocatalysts in advanced oxidation processes for wastewater purification: challenges and future prospects, Catalysts. 12 (7) (2022) 741.
[11] K.F. Ngulube, A. Abdelhaleem, M. Fujii, M. Nasr, Synergism of artificial intelligence and techno-economic for sustainable treatment of methylene blue dye-containing wastewater by photocatalysis, Sustainability. 16 (2) (2024) 529.
[12] K.M. Lee, C.W. Lai, K.S. Ngai, J.C. Juan, Recent developments of zinc oxide based photocatalyst in water treatment technology: a review, Water. Res. 88 (2016) 428–448.
[13] F.M. Sanakousar, C.C. Vidyasagar, V.M. Jiménez-Pérez, K. Prakash, Recent progress on visible-light-driven metal and non-metal doped ZnO nanostructures for photocatalytic degradation of organic pollutants, Mater. Sci. Semicond. Process. 140 (2022) 106390.
[14] T.V.H. Luu, N.T.M. Tho, T.T.T. Thuy, L.N. Thong, N.T. Dung, P.H. Dang, Synthetization pill-like C-doped ZnO nano-photocatalyst for removing ofloxacin and methylene blue under visible light, J. Sol-Gel Sci. Technol. 110 (1) (2024) 204–220.
[15] N. Turkten, M. Bekbolet, Photocatalytic performance of titanium dioxide and zinc oxide binary system on degradation of humic matter, J. Photochem. Photobiol. A 401 (2020).
[16] N. Turkten, Y. Karatas, M. Bekbolet, Preparation of PANI modified ZnO composites via different methods: structural, morphological and photocatalytic properties, Water. (Basel) 13 (8) (2021).
[17] N. Turkten, Y. Karatas, M. Bekbolet, Conducting polymers and photocatalysis: a mini review on selected Conducting polymers and photocatalysts as TiO_2 and ZnO, Journal of Photocatalysis 2 (4) (2021) 252–270.
[18] H. AlMohamadi, S.A. Awad, A.K. Sharma, N. Fayzullaev, A. Távara-Aponte, L. Chiguala-Contreras, A. Amari, C. Rodriguez-Benites, M.A. Tahoon, H. Esmaeili, Photocatalytic activity of metal- and non-metal-anchored ZnO and TiO_2 nanocatalysts for advanced photocatalysis: comparative study, Catalysts. 14 (7) (2024) 420.
[19] R.R. Wary, M. Narzary, B.B. Brahma, D. Brahma, P. Kalita, M.Buzar Baruah, Nanostructural design of ZnO using an agro-waste extract for a sustainable process and its photocatalytic activity, ACS. Appl. Bio Mater. 6 (11) (2023) 4645–4661.
[20] S.N.U.S. Bukhari, A.A. Shah, M.A. Bhatti, A. Tahira, I.A. Channa, A.K. Shah, A. D. Chandio, W.A. Mahdi, S. Alshehri, Z.H. Ibhupoto, W. Liu, Psyllium-husk-assisted synthesis of ZnO microstructures with improved photocatalytic properties for the degradation of methylene blue (MB), Nanomaterials 12 (20) (2022) 3568.
[21] N.P.F. Gonçalves, M.A.O. Lourenço, S.R. Baleuri, S. Bianco, P. Jagdale, P. Calza, Biochar waste-based ZnO materials as highly efficient photocatalysts for water treatment, J. Environ. Chem. Eng. 10 (2) (2022) 107256.
[22] J.Y. Loke, R.S. Mohd Zaki, H.D. Setiabudi, Photocatalytic degradation of methylene blue using ZnO supported on wood waste-derived activated carbon (ZnO/AC), Mater. Today Proc. 57 (2022) 1315–1321.
[23] K. Bhardwaj, A.K. Singh, Bio-waste and natural resource mediated eco-friendly synthesis of zinc oxide nanoparticles and their photocatalytic application against dyes contaminated water, Adv. Chem. Eng. 16 (2023) 100536.
[24] I. Moroz, L.G.B. Scapolio, I. Cesarino, A.L. Leão, G. Bonanomi, Toxicity of cigarette butts and possible recycling solutions—A literature review, Environ. Sci. Pollut. Res. 28 (9) (2021) 10450–10473.
[25] Ç. Deniz İzlen, Co–Fe Co-doped activated carbon from waste cigarette filters for color and COD removal from textile wastewater, J. Water Chem. Technol. 45 (2) (2023) 120–127.
[26] A. Gupta, O.P. Pandey, Visible irradiation induced photodegradation by NbC/C nanocomposite derived from smoked cigarette litter (filters), Sol. Energy 163 (2018) 167–176.
[27] L.P. Glugoski, P. de Jesus Cubas, S.T. Fujiwara, Reactive black 5 dye degradation using filters of smuggled cigarette modified with Fe^{3+}, Environ. Sci. Pollut. Res. 24 (7) (2017) 6143–6150.
[28] S.P. Onkani, P.N. Diagboya, F.M. Mtunzi, M.J. Klink, B.I. Olu-Owolabi, V. Pakade, Comparative study of the photocatalytic degradation of 2–chlorophenol under UV irradiation using pristine and Ag-doped species of TiO_2, ZnO and ZnS photocatalysts, J. Environ. Manag. 260 (2020) 110145.
[29] P. Scherrer, Estimation of the size and internal structure of colloidal particles by means of röntgen, Nachr. Ges. Wiss. Gottingen 2 (1918) 96–100.
[30] A. De Fenzo, M. Giordano, L. Sansone, A clean process for obtaining high-quality cellulose acetate from cigarette butts, Materials. (Basel) 13 (21) (2020).
[31] R. Li, X. Tian, M. Wei, A. Dong, X. Pan, Y. He, X. Song, H. Li, Flexible pressure sensor based on cigarette filter and highly conductive MXene sheets, Compos. Commun. 27 (2021) 100889.
[32] W. Li, X. Tian, X. Li, J. Liu, C. Li, X. Feng, C. Shu, Z.-Z. Yu, An environmental energy-enhanced solar steam evaporator derived from MXene-decorated cellulose acetate cigarette filter with ultrahigh solar steam generation efficiency, J. Colloid. Interface Sci. 606 (2022) 748–757.
[33] E. Abu-Danso, A. Bagheri, A. Bhatnagar, Facile functionalization of cellulose from discarded cigarette butts for the removal of diclofenac from water, Carbohydr. Polym. 219 (2019) 46–55.
[34] T.G. Kazi, N. Jalbani, M.B. Arain, M.K. Jamali, H.I. Afridi, R.A. Sarfraz, A.Q. Shah, Toxic metals distribution in different components of Pakistani and imported cigarettes by electrothermal atomic absorption spectrometer, J. Hazard. Mater. 163 (1) (2009) 302–307.
[35] K.S.W. Sing, Reporting physisorption data for gas/solid systems with special reference to the determination of surface area and porosity (Recommendations 1984), Pure Appl. Chem. (1985) 603.
[36] K.V. Karthik, A.V. Raghu, K.R. Reddy, R. Ravishankar, M. Sangeeta, N.P. Shetti, C. V. Reddy, Green synthesis of Cu-doped ZnO nanoparticles and its application for the photocatalytic degradation of hazardous organic pollutants, Chemosphere 287 (2022) 132081.
[37] V. Gilja, I. Vrban, V. Mandic, M. Zic, Z. Hrnjak-Murgic, Preparation of a PANI/ZnO composite for efficient photocatalytic degradation of acid bue, Polymers. (Basel) 10 (9) (2018).
[38] C.-C. Hwang, T.-Y. Wu, Synthesis and characterization of nanocrystalline ZnO powders by a novel combustion synthesis method, Mater. Sci. Eng. B 111 (2) (2004) 197–206.
[39] B.K. Tripathy, S. Kumar, M. Kumar, A. Debnath, Microwave induced catalytic treatment of brilliant green dye with carbon doped zinc oxide nanoparticles: central composite design, toxicity assessment and cost analysis, Environ. Nanotechnol. Monit. Manage 14 (2020) 100361.
[40] A. Top, H. Çetinkaya, Zinc oxide and zinc hydroxide formation via aqueous precipitation: effect of the preparation route and lysozyme addition, Mater. Chem. Phys. 167 (2015) 77–87.
[41] A.S. Lanje, S.J. Sharma, R.S. Ningthoujam, J.S. Ahn, R.B. Pode, Low temperature dielectric studies of zinc oxide (ZnO) nanoparticles prepared by precipitation method, Adv. Powder. Technol. 24 (1) (2013) 331–335.
[42] Y. Ding, L. Niu, Y. Chen, M. Wang, Study on the defect structure of carbon-doped ZnO materials, Cryst. Res. Technol 58 (5) (2023) 2300015.
[43] O. Bechambi, S. Sayadi, W. Najjar, Photocatalytic degradation of bisphenol A in the presence of C-doped ZnO: effect of operational parameters and photodegradation mechanism, J. Ind. Eng. Chem. 32 (2015) 201–210.
[44] S. Yurdakal, C. Garlisi, L. Özcan, M. Bellardita, G. Palmisano, Chapter 4 - (Photo) catalyst characterization techniques: adsorption isotherms and BET, SEM, FTIR, UV–Vis, photoluminescence, and electrochemical characterizations, in: G. Marcì, L. Palmisano (Eds.), Heterogeneous Photocatalysis, Elsevier, 2019, pp. 87–152.
[45] I. Limón-Rocha, C.A. Guzmán-González, L.M. Anaya-Esparza, R. Romero-Toledo, J. L. Rico, O.A. González-Vargas, A. Pérez-Larios, Effect of the precursor on the synthesis of ZnO and its photocatalytic activity, Inorganics. (Basel) 10 (2) (2022) 16.
[46] S. Labuayai, V. Promarak, S. Maensiri, Synthesis and optical properties of nanocrystalline ZnO powders prepared by a direct thermal decomposition route, Appl. Phys. A 94 (4) (2009) 755–761.
[47] D.A. Oluwasogo, S. Varangane, Y.T. Prabhu, B.M. Abraham, V. Perupogu, U. Pal, Biosynthetic modulation of carbon-doped ZnO for rapid photocatalytic endocrine disruptive remediation and hydrogen evolution, J. Clean. Prod. 394 (2023) 136393.
[48] M.A. Rauf, M.A. Meetani, A. Khaleel, A. Ahmed, Photocatalytic degradation of Methylene Blue using a mixed catalyst and product analysis by LC/MS, Chem. Eng. J. 157 (2) (2010) 373–378.
[49] X. Liu, Y. Yang, X. Shi, K. Li, Fast photocatalytic degradation of methylene blue dye using a low-power diode laser, J. Hazard. Mater. 283 (2015) 267–275.
[50] S. Akir, A. Hamdi, A. Addad, Y. Coffinier, R. Boukherroub, A.Dakhlaoui Omrani, Facile synthesis of carbon-ZnO nanocomposite with enhanced visible light photocatalytic performance, Appl. Surf. Sci. 400 (2017) 461–470.
[51] H. Xiao, Y. Shan, W. Zhang, L. Huang, L. Chen, Y. Ni, B. Boury, H. Wu, C-nanocoated ZnO by TEMPO-oxidized cellulose templating for improved photocatalytic performance, Carbohydr. Polym. 235 (2020) 115958.
[52] S. Luo, C. Liu, S. Zhou, W. Li, C. Ma, S. Liu, W. Yin, H.J. Heeres, W. Zheng, K. Seshan, S. He, ZnO nanorod arrays assembled on activated carbon fibers for photocatalytic degradation: characteristics and synergistic effects, Chemosphere 261 (2020) 127731.